Materials Today Physics 27 (2022) 100797

Contents lists available at ScienceDirect

Materials Today Physics

journal homepage: www.journals.elsevier.com/materials-today-physics

Simultaneous optical resonances at visible and mid-infrared frequencies with epitaxial TiN/$Al_{0.72}Sc_{0.28}N$/TiN metal/polar-dielectric/metal multilayers

Krishna Chand Maurya [a,b], Ashalatha Indiradevi Kamalasanan Pillai [c], Magnus Garbrecht [c], Bivas Saha [a,b,d,*]

[a] Chemistry and Physics of Materials Unit, Jawaharlal Nehru Centre for Advanced Scientific Research, Bangalore, 560064, India
[b] International Centre for Materials Science, Jawaharlal Nehru Centre for Advanced Scientific Research, Bangalore, 560064, India
[c] Sydney Microscopy & Microanalysis, The University of Sydney, NSW, 2006, Australia
[d] School of Advanced Materials, Jawaharlal Nehru Centre for Advanced Scientific Research, Bangalore, 560064, India

ARTICLE INFO

Keywords:
Fabry-Pérot cavity
Berremann modes
Metal/polar-insulator/metal heterostructures
Super absorbers
Mid-infrared photonics

ABSTRACT

Traditionally, light-matter interactions in the visible spectral range utilize tailored plasmonic nanostructure in metals that often require advanced nanofabrication techniques. Concomitantly, polar lattice vibrations in dielectrics are used to achieve mid-to-long wavelength infrared (IR) light-matter coupling. Achieving optical resonances simultaneously in the visible and mid-to-long wavelength IR spectral range in one host medium has been challenging due to mutually conflicting material and optical property requirements. In this article, we show simultaneous light-matter coupling and development of super absorbers in the visible and mid-IR spectral ranges with a lithography-free planar wide-angle metal-(polar)-dielectric-metal (MDM) Fabry-Pérot cavity composed of ultrathin refractory metallic TiN as the top layer and polar dielectric $Al_{0.72}Sc_{0.28}N$ as the spacer layer. Lattice-matched TiN/$Al_{0.72}Sc_{0.28}N$/TiN MDM cavities exhibit super absorption resonance with maximum absorptivity of ~99%. The absorption maxima spectral position is tuned with changes in spacer layer thickness and by utilizing multiple cavity interactions. $Al_{0.72}Sc_{0.28}N$ inside the MDM is also used for light coupling to the transverse optical phonon mode and to the Berremann mode near the longitudinal phonon frequency with strong selective absorption. Demonstration of refractory epitaxial TiN/$Al_{0.72}Sc_{0.28}N$/TiN MDM metamaterials mark significant progress towards developing compact optical meta-structures with on-demand optical resonances at different spectral ranges.

Artificially structured metamaterials provide unprecedented opportunities to control light-matter interactions at the nanoscale and lead to a plethora of device applications. Light-matter interactions in the visible and near-IR spectral ranges are utilized for various device technologies such as photovoltaics [1,2], photodetectors [3], photocatalysis [4], phototransistors [5], light emitting diodes (LEDs) [6], and electro-optic modulator [7,8]. At the same time, in recent years infrared light-matter coupling is becoming increasingly important for many other emerging device applications such as radiative cooling [9,10], thermophotovoltaics [11–13], telecommunication [14], sensing [15], and surveillance [16,17]. Therefore, materials and structures that demonstrate simultaneous light-matter interactions and optical resonances in the visible and in mid-to-long wavelength IR spectral ranges would usher in a new era of compact multifunctional device technologies [18].

Traditionally, light-matter interactions in the visible and near IR spectral range utilize plasmon resonance on metals and surface-plasmon-polaritons at metal/dielectric interfaces [19] [–] [21]. Various self-assembled and patterned nanostructures have been also employed for nanophotonic applications [22] [–] [24]. Plasmonic nanostructures have been used to achieve sub-wavelength light confinement, field localization, refractive index control, phase and amplitude control and others [25,26]. Many device functionalities such as perfect absorbers over a broad spectral range, or wavelength-selective perfect emitters, were demonstrated [27] [–] [29]. Also, the planar multilayer structures have attracted significant interest for high absorptions using Tamm plasmon resonances (TP) [30,31], coherent

* Corresponding author. Chemistry and Physics of Materials Unit, Jawaharlal Nehru Centre for Advanced Scientific Research, Bangalore, 560064, India.
E-mail addresses: bsaha@jncasr.ac.in, bivas.mat@gmail.com (B. Saha).

https://doi.org/10.1016/j.mtphys.2022.100797
Received 10 May 2022; Received in revised form 29 June 2022; Accepted 22 July 2022
Available online 8 August 2022

perfect absorption (CPA) [32,33] etc. The Tamm resonances can be achieved at the surface between a periodic dielectric structure (Bragg mirror) and a metallic layer, while the CPA can be achieved in MDM structure by optimizing the thickness and permittivity of the metal-dielectric layers. However, tailored optical resonances in most of these devices are usually achieved with nanostructures that often require advanced lithography and nanofabrication methods [27] [–] [29,34]. Moreover, spectral selectivity and device performance are strongly dependent on the periodicity, size and shape of these nanostructures, which limits their application space.

Similarly, optical resonance in the mid-to-long wavelength IR spectral range utilizes polar dielectrics, where the electromagnetic wave can couple to the polar lattice vibrations [35] [–] [37]. Owing to the transverse nature of the electromagnetic wave, light couples directly to the transverse optical (TO) phonon modes in polar dielectrics such as AlN [38], SiC [39], GaN [40], ScN [41,42], and leads to the phonon-polaritons (a hybrid quasiparticle made of photons and phonons) formations. As a result of such coupling, polar dielectrics exhibit negative dielectric permittivity within a frequency range, known as the Reststrahlen band that is encompassed by the transverse optical (TO) and longitudinal optic (LO) phonon modes [43]. Due to the negative permittivity, polar dielectrics behave like conventional metals and reflect incident radiation strongly within the Reststrahlen band. Along with the direct coupling and optical absorption with the TO phonon modes, electromagnetic modes can also couple to the leaky polaritonic Berreman modes [44,45] near the LO phonon frequency in planar polar dielectric films deposited on metal surfaces. Coupling of light with such Berreman mode also leads to optical absorptions and is proposed for selective emitter design in the mid-IR spectral ranges.

Therefore, (meta)-materials or (meta)-structures that can utilize the light-matter interactions over the visible to long-wavelength IR spectral range could lead to many hybrid device functionalities that no individual materials can provide [18]. Yet, despite the apparent benefits very little progress has been in this pursuit primarily due to the materials incompatibility and nanofabrication challenges. For example, noble metals such as Ag and Au are used for the plasmon resonance in the near-UV-to-visible spectral ranges. However, as noble metals do not possess optical phonon modes, they do not lead to optical resonances in the mid-to-long wavelength IR spectral ranges. Similarly, though polar dielectrics exhibit the light-matter coupling in the mid-to-long wavelength IR spectral ranges, they do not show plasmonic response due to the absence of carriers. Noble metals are also soft and unstable at high temperatures, which compounds this fundamental material incompatibility challenge [20]. Due to their high surface energies, noble metals cannot be deposited in thin-film and ultrathin film with low roughness. At the same time, noble metals are not compatible with complementary-metal-oxide-semiconducting (CMOS) technologies and are not suitable for epitaxial heterostructure development without atomic intermixing at the interfaces [46].

With the emergence of transition metal nitrides (TMNs) as alternative plasmonic materials [20,41,47,48], the situation has improved substantially. TMNs such as TiN are mechanically hard, corrosion-resistant, exhibit a high melting temperature, and can be deposited in ultrathin films with low surface roughness [49,50]. Planar epitaxial TiN/$Al_{0.72}Sc_{0.28}N$ metal/dielectric superlattices with nanoscale period thicknesses have been developed that exhibit hyperbolic photonic dispersion and a significantly enhanced photonic density of states, as well as tunable plasmonic resonances [51,52]. Such superlattice metamaterials are also found to be stable at high-temperatures for an extended period of time [53,54]. While TiN in TiN/$Al_{0.72}Sc_{0.28}N$ metamaterials act as the metallic component, it is also important to note that $Al_{0.72}Sc_{0.28}N$ is a polar dielectric that can support optical resonances in the mid-to-long wavelength IR spectral range. AlN, which is the parent material of $Al_xSc_{1-x}N$, is a well-known polar dielectric with the TO and LO phonon mode frequencies at 673 cm^{-1} and 890 cm^{-1}, respectively. Though the inclusion of scandium inside AlN is necessary for stabilizing $Al_xSc_{1-x}N$ in the rocksalt phase [55], and for the lattice-matching with TiN, it does not change AlN's polar semiconducting nature considerably.

In this work, motivated by the idea of creating simultaneous optical resonances in the visible and mid-to-long wavelength IR spectral ranges, we demonstrate epitaxial TiN/$Al_{0.72}Sc_{0.28}N$/TiN MDM Fabry-Pérot cavity that not only results in tunable super absorption in the 500–1200 nm spectral range but also exhibit narrow-band selective absorption/emission corresponding to $Al_{0.72}Sc_{0.28}N$'s TO phonon mode and Berreman mode frequencies. Importantly, we achieve three different types of resonances, namely Fabry-Pérot cavity resonance [30], light coupling to the polar TO phonon modes and to the Berreman modes [56] in one planar, lithography-free large-area CMOS compatible MDM structure deposited on insulating substrates that can be seamlessly integrated with devices.

TiN/$Al_{0.72}Sc_{0.28}N$/TiN MDM Fabry-Pérot cavity heterostructures are fabricated on (001) MgO substrates with dc-magnetron sputtering inside an ultrahigh vacuum chamber at a base pressure of 2×10^{-9} Torr. All growths are performed at 10 mTorr deposition pressure at a substrate temperature of 800 $^{\circ}C$. Details about the growth method are presented in Supplementary Information (SI) section 1. Structural properties of the heterostructure metamaterials determined with high-resolution (scanning) transmission electron microscopy (HR(S)/TEM) imaging (see Fig. 1 for a representative double cavity structure) show that the TiN and $Al_{0.72}Sc_{0.28}N$ layers grow with cubic epitaxy on (001) MgO surfaces. The 100 nm thick bottom TiN layer serves as the back mirror for light reflection and grows with lattice-matched epitaxy. The $Al_{0.72}Sc_{0.28}N$ layers are homogeneous, uniform and exhibit very little interface roughness with TiN (see Fig. 1(b)). The atomic resolution STEM image in Fig. 1(c) shows coherent growth of $Al_{0.72}Sc_{0.28}N$ layers on TiN with [001] (001) $Al_{0.72}Sc_{0.28}N$ || [001] (001) TiN epitaxial relationship. The STEM energy dispersive x-ray spectroscopy (EDS) analysis show Ti, Al, and Sc have not been diffusing between the layers during growth. Due to the x-ray emission peak overlap between Sc and N, the N map shows slight inhomogeneities.

MDM cavities are fabricated with a 100 nm TiN as the bottom layer for super absorber design in the visible spectral range. The top TiN layer thickness is kept constant at 15 nm, while the $Al_{0.72}Sc_{0.28}N$ spacer layer thickness is varied from 50 nm to 100 nm and 150 nm (see Fig. 2(a)). Reflectivity (R) measurements (see SI Fig. S2) show clear reflection dips at 580 nm, 810 nm, and 1000 nm for the MDM cavities when the dielectric layer thickness ranges from 50 nm to 100 nm–150 nm, respectively. As the bottom TiN layer is optically opaque with zero transmission, the absorptivity (A) of the structures is calculated from the reflectivity spectrum with $A = 1\text{-}R$ ($T = 0$) relationship. Absorption spectra show that all the three cavity structures exhibit very high absorption maxima at 99%, 97%, and 97% respectively (see Fig. 2(b)). It is also important to note that the absorption maxima in the three structures cover a large portion of the visible-to-near-IR spectral range (580 nm–1200 nm). A higher-order absorption peak starts to appear at ~480 nm for the MDM cavity with a spacer layer thickness of 150 nm.

The MDM cavities' absorption spectra are simulated with the finite element method (FEM). The complex dielectric constants of the bottom 100 nm and top 15 nm TiN, and $Al_{0.72}Sc_{0.28}N$ spacer layers are obtained with spectroscopic ellipsometry measurements (see SI section-4 for details). The real component of the dielectric permittivity (ε_1) of TiN shows a positive-to-negative transition at ~ 480 nm that corresponds to the wavelength associated with TiN's plasma frequency. The optical losses, represented by the imaginary component of the dielectric permittivity (ε_2) of TiN, increase with an increase in the wavelength due to free-electron Drude scattering. The wavelength corresponding to the plasma frequency and dielectric permittivity of TiN is comparable to previous reports [20,47,48]. $Al_{0.72}Sc_{0.28}N$ spacer layers, on the other hand, exhibit nearly constant permittivity above 500 nm that is consistent with its dielectric nature. Due to the direct bandgap of $Al_{0.72}Sc_{0.28}N$ of ~3.4 eV, Lorentz peaks are observed in both spectrums

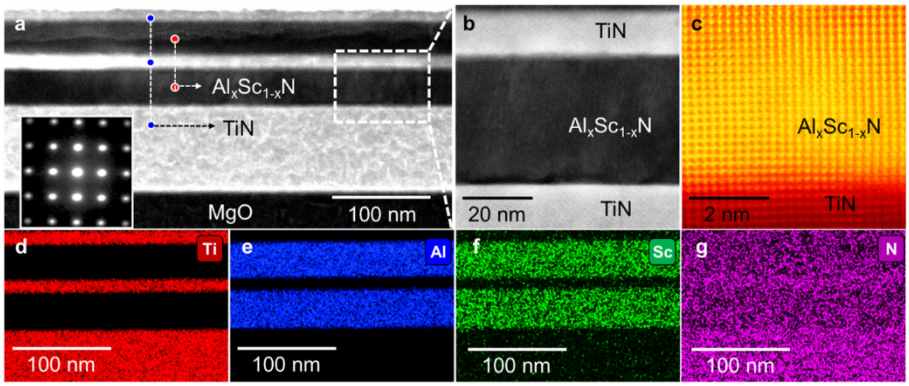

Fig. 1. a) STEM micrograph of TiN/$Al_{0.72}Sc_{0.28}N$ multilayer stack deposited on (001) MgO is presented. Coherent epitaxial interfaces between different layers are visible in the images. The electron diffraction pattern in the inset confirms the lattice-matched cubic epitaxial growth. b) High-magnification STEM image highlight the TiN/$Al_{0.72}Sc_{0.28}N$ interfaces. c) Atomic resolution STEM image of the TiN/$Al_{0.72}Sc_{0.28}N$ interface is presented demonstrating a sharp interface. STEM-EDS elemental mapping of d) Ti, e) Al, f) Sc, and g) N demonstrates well-separated layers without diffusion of atoms into adjacent layers.

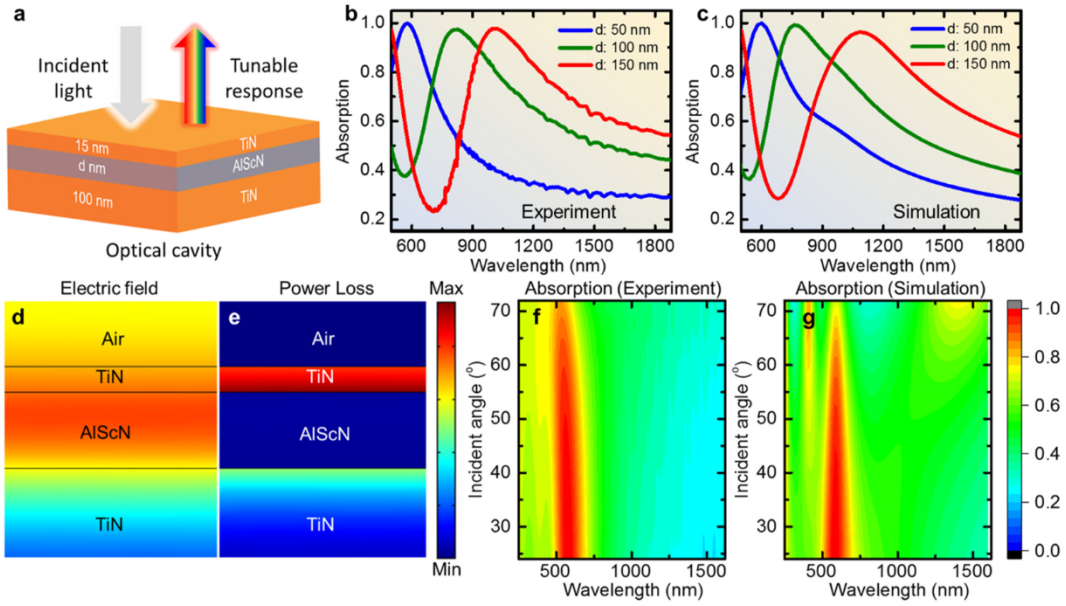

Fig. 2. a) Schematic diagram of the unit cell of metal-dielectric-metal (MDM) optical cavity. b) Experimental and c) simulated absorption spectra of the MDM structures with varying dielectric $Al_{0.72}Sc_{0.28}N$ layer thickness (50 nm (blue), 100 nm (green), 150 nm (red)). d) Magnitude of electric field profile and (e) electromagnetic power-loss density distribution for the MDM structure (50 nm of $Al_{0.72}Sc_{0.28}N$ thickness) at the maximum absorption peak wavelength of 580 nm. f) Experimental and g) simulated angle-dependent absorption curve of MDM structure (of 50 nm thick $Al_{0.72}Sc_{0.28}N$).

(see Fig. S1 (b)). Notably, the optical losses of $Al_{0.72}Sc_{0.28}N$ are negligible above 500 nm spectral range. As shown in Fig. 2(c), the calculated absorption spectra of MDM structures match the experimental results. The peak positions, peak-width, and peak-shape are nearly identical between the experiment and simulated results.

Unlike the spectrally selective absorbers that use the plasmon resonances, the super absorbers developed in this work utilize light interference inside the MDM cavity. The Fabry-Pérot cavity with a nearly lossless dielectric spacer layer bounded by the optically thick bottom metallic TiN and thin top TiN layer supports the coherent perfect absorption (CPA). The behavior of the cavity resonance can be described qualitatively by the resonance condition [30].

$$2\left(\frac{2\pi}{\lambda_{res}}\right)n_d t_d + \varphi_{Bottom-TiN} + \varphi_{Top-TiN} = 2m\pi \quad (1)$$

The first term on the left side of the equation represents the round-trip propagation phase shift within the cavity. Where n_d and t_d are the refractive index and thickness on the dielectric $Al_{0.72}Sc_{0.28}N$ layer, respectively. λ_{res} is the resonance wavelength and m is an integer number determining the order of cavity mode. $\varphi_{Bottom-TiN}$ and $\varphi_{Bottom-TiN}$ are the phase shifts upon reflection at the bottom and top metal−dielectric interfaces, respectively. The FEM simulation-derived electric field distributions show the underlying mechanism more clearly. Fig. 2 (d) shows that the electric field is highly confined inside the $Al_{0.72}Sc_{0.28}N$ spacer layer due to the formation of standing waves. Constructive interference between the incoming and reflected light leads to such effects with the field maxima located at the center of the spacer layer. Since the electric field is maximum at the middle of the spacer layer, most energy is absorbed in the top metal layer and at the bottom spacer/metal interfaces, as shown in Fig. 2(e).

Further, the origin of the optical resonance of the MDM structures is explained using a quantum mechanical description of the MDM cavity as a double barrier quantum well and the classical harmonic oscillator model (as presented in detail in reference [57,58]). TiN is found to satisfy the Hermiticity limit to obtain the resonances by resonant tunnelling through the metal (see SI figure S6). On the other hand, using the effective dielectric permittivity obtained from the classical harmonic oscillator, we show that the cavity resonance corresponds to the epsilon-near-zero (ENZ) mode of the MDM structures (see the SI section-9 and section-10 for the detailed analysis). Both the classical oscillator and the quantum mechanical approaches exhibit very good agreement with the experimental results.

Angle-dependent absorption is further measured (see Fig. 2(f)), and its numerical simulation results are presented in Fig. 2(g). The super absorption peak is visible at all angles of incidence (° $24^0 - 72^0$). However, the super absorption intensity decreases with an increase in the angles of incidence. From the measured absorption spectra (Fig. 2 (b)), a resonance full-width-half-maxima (FWHM) of 175 nm, 324 nm, and 367 nm is calculated that lead to a quality factor (*Q*-factor) of 3.3, 2.5, and 2.7 for the three MDM structures with 50 nm, 100 nm, and 150 nm spacer layer thicknesses. Though the *Q*-factors ($\lambda/\Delta\lambda$) are rather low, it is a manifestation of the higher optical loss of TiN compared to noble metals such as Ag and Ag [59]. While a narrowband absorber is generally useful for sensing, imaging and color filter applications [59] [–] [61], the slightly broadband TiN-based absorber can be useful for thermal photovoltaics, radiative cooling, photodetectors, etc. [62,63] Since the dielectric properties of TiN can also be tuned with growth conditions, a narrowband absorber can be achieved by reducing the optical loss of the metallic TiN. Also, it is known that the cavity mode can be tailored by ultrafast optical pumping, which increases the local permittivity and results in a redshift in the resonance mode [64]. This approach can be useful for the TiN/$Al_{0.72}Sc_{0.28}N$/TiN MDM multilayer structure as well, which will further the progress in ultrafast manipulation of optical nonlinearities, such as high harmonic generation and other ultrafast light-driven technologies.

Besides demonstrating tunable absorption in the visible spectral range, optical resonance engineering is performed through multi-cavity interactions. An additional 50 nm $Al_{0.72}Sc_{0.28}N$ spacer layer and 15 nm thick TiN layer are deposited on the existing MDM structure with 50 nm $Al_{0.72}Sc_{0.28}N$ spacer layer (see Fig. 3(a)). The first-order mode at 580 nm splits into two at ~ 440 nm (λ_1) and ~ 690 nm (λ_2) (see Fig. 3(c)). Such splitting of the modes due to multi-cavity interactions [58,65] is an effective way to achieve tailored absorptions in the desired spectral ranges and is well-supported by the simulation results (see Fig. 3(d)). Simulation results show that corresponding to the first split peak at ~440 nm, the electric field is highly confined in cavity 2 (or the bottom cavity spacer layer). Whereas the electric field is found to be maximum at the $Al_{0.72}Sc_{0.28}N$ spacer layer inside cavity 1 for the second peak located at ~690 nm (see Fig. 3(e) and (f)). Similarly, most of the energy is absorbed in the top and middle TiN layers as well as at the TiN/$Al_{0.72}Sc_{0.28}N$ interfaces as Fig. 3(g) and (h) show. Higher-order cavity mode splitting experiments and simulations are further performed, and the results are presented in the SI section-8. This splitting of optical modes due to the interactions among multiple cavities is analogous to the formation of bonding and antibonding orbitals in the molecular orbital theory [66,67].

Having demonstrated super absorbers in the visible spectral range with MDM Fabry-Pérot cavities, we focus on achieving selective absorption at the mid-IR frequencies. The absorption spectrum of the cavity structures in the mid-to-long wavelength IR is measured with a Fourier Transform Infrared spectrometer (FTIR). Since the bottom 100 nm TiN is optically opaque for light transmission in the entire mid-to-long wavelength IR, reflectivity (R) measurements and subsequent utilization of the A = 1-R relationship are used to obtain the absorption. MDM cavity with 100 nm $Al_{0.72}Sc_{0.28}N$ spacer layer exhibits an absorption peak at 891 cm^{-1} (see Fig. 4(a)) corresponding to the Berreman mode excitation near the $Al_{0.72}Sc_{0.28}N$'s LO phonon frequency (discussed in detail subsequently). The FWHM of the absorption peak is 62 cm^{-1}, which results in a measured *Q*-factor of 14. Similarly, cavities with 50 nm and 150 nm $Al_{0.72}Sc_{0.28}N$ spacer layers exhibit selective absorption due to the Berreman mode excitations (see SI Fig. S10). It is important to note that the Berreman mode mid-IR absorption is visible in these MDM metamaterials despite the presence of a 15 nm TiN on top of the $Al_{0.72}Sc_{0.28}N$ spacer layer. Removal of the top TiN layer increases the absorption coefficient slightly (as shown in Fig. 4(a). These results, therefore, show that the MDM Fabry-Pérot cavities exhibit simultaneous visible and mid-IR light absorption (as shown in Fig. 4(b)).

Detailed experiments and modeling are performed to determine the absorption mechanism. Reflectivity measurement *(R)* of (001) MgO substrates show a clear and well-defined Reststrahlen band with more than 90% of the incident light reflected within the band. From the fitting of the reflectivity spectrum with the Fresnel equation, TO and LO phonon frequencies of 395 cm^{-1} and 795 cm^{-1} are determined for MgO (see Fig. 5(a)) which is consistent with literature reports [68]. Similarly, when a thick 200 nm AlN (parent polar dielectric $Al_{0.72}Sc_{0.28}N$) layer is deposited on (001) MgO substrate, two distinct Reststrahlen bands are observed in the reflectivity spectrum. One of the Reststrahlen bands corresponds to MgO, while the other results from light reflection from the AlN Reststrahlen band. Fitting the spectrum with the Fresnel equation further shows that an LO and TO phonon frequency of 673 cm^{-1} and 896 cm^{-1} for AlN is consistent with previous reports [69]. With the demonstration of the Reststrahlen bands, 200 nm AlN layer is deposited

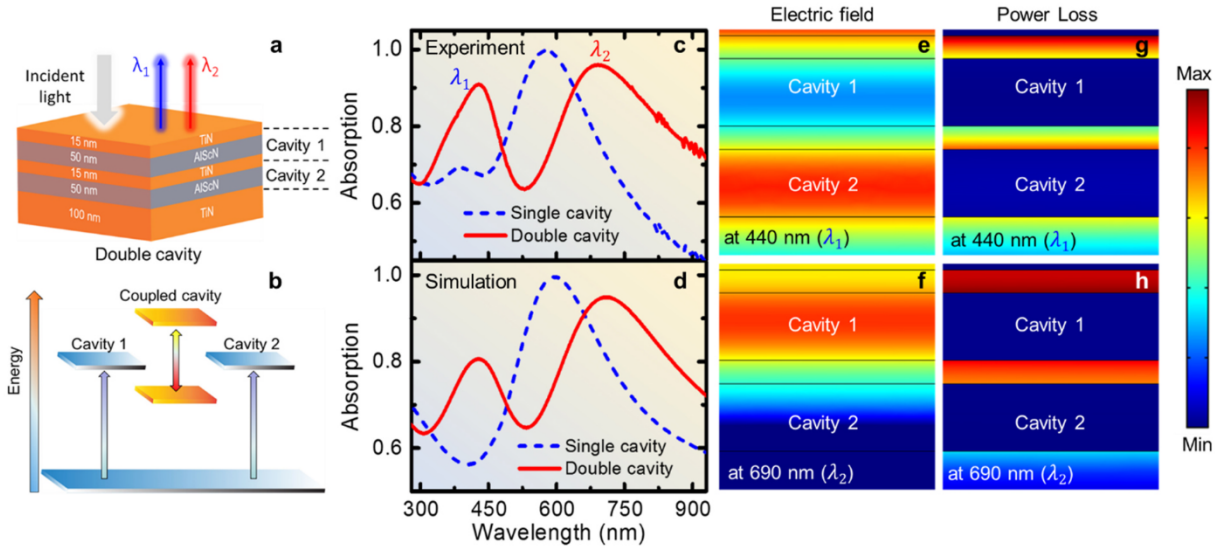

Fig. 3. a) Schematic diagram of TiN/$Al_{0.72}Sc_{0.28}N$ based double cavity structure. b) Schematic diagram that shows the splitting of energy states due to the coupling between double cavities. c) Experimental and d) simulated absorption spectra of double cavity mode (red line) along with the single cavity mode (blue dash line). The splitting of the curve corresponds to the direct coupling of the two cavities. (e, f) Magnitude of electric field profile and (g, h) electromagnetic power-loss density distribution for the double cavity (50 nm of $Al_{0.72}Sc_{0.28}N$ thickness) at the maximum absorption peak wavelength of 440 nm and 690 nm.

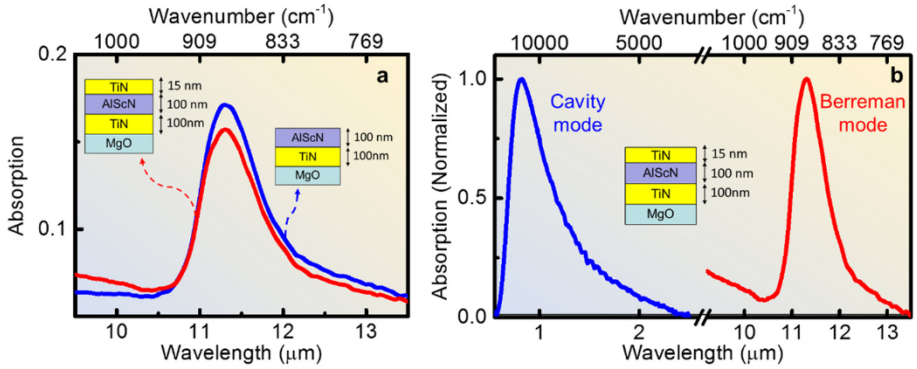

Fig. 4. Effect of TiN top-layer on $Al_{0.72}Sc_{0.28}N$/TiN/MgO sample in IR and visible range. a) FTIR reflection of $Al_{0.72}Sc_{0.28}N$/TiN/MgO and TiN/$Al_{0.72}Sc_{0.28}N$/TiN/MgO samples. Thin TiN (15 nm) top layer film does not affect the optical phonon much, while strong absorption in the visible range appeared due to the cavity resonance. (b) Simultaneous optical resonances, cavity mode and Berreman mode can be achieved in MDM structures.

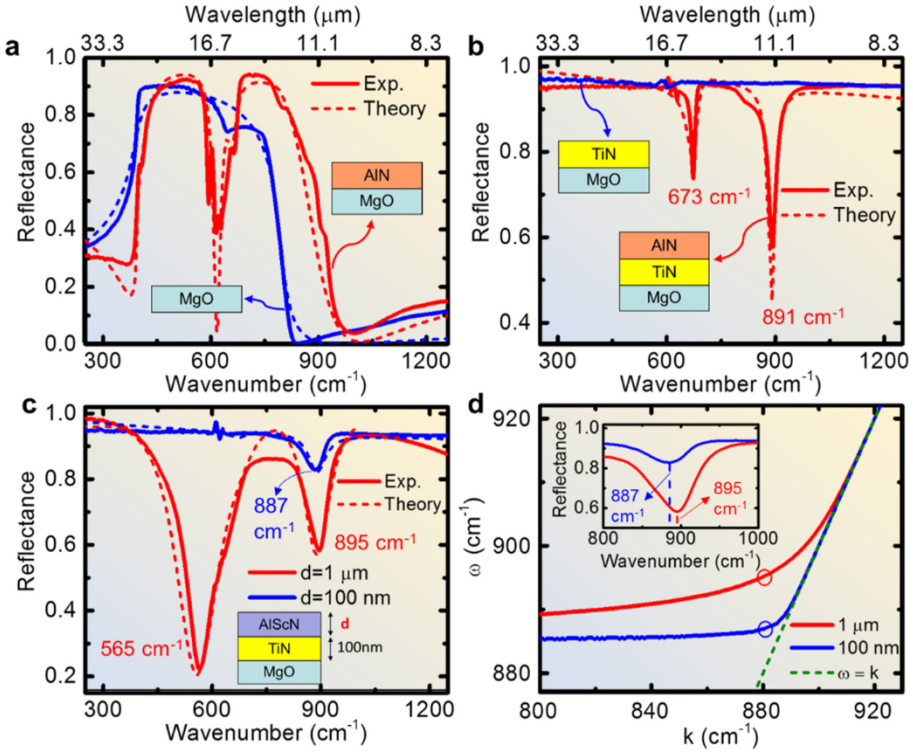

Fig. 5. FTIR Reflection spectra are collected from a) AlN/MgO (red) along with MgO substrate (blue). For MgO substrate, a clear Reststrahlen band spread over 395 cm^{-1} to 767 cm^{-1}. For the sample AlN/MgO, two Reststrahlen bands appeared from AlN and MgO. b) Reflection spectra of TiN/MgO and AlN/TiN/MgO. Metal TiN reflectivity is around 95% in the whole FTIR spectral range. For the sample AlN/TiN/MgO, two dips in the reflection spectra correspond to the absorption of TO and LO phonon of AlN. c) IR-reflection of $Al_{0.72}Sc_{0.28}N$/TiN/MgO samples of two different thicknesses of $Al_{0.72}Sc_{0.28}N$ 100 nm and 1000 nm is compared. Two dips in the reflection spectra correspond to the TO and LO modes appearing in the thicker $Al_{0.72}Sc_{0.28}N$ while the optical modes are barely visible in the thinner film. d) Berreman mode dispersion relationship for 100 nm (blue) and 1 μm (red) thick $Al_{0.72}Sc_{0.28}N$/TiN samples calculated using Eq. (3). The light line is shown as a dotted green line. The inset shows the Berreman mode of $Al_{0.72}Sc_{0.28}N$ films.

on a 100 nm TiN base-layer on (001) MgO substrate. Such metal/polar-dielectric structures are known to support leaky modes known as Berreman modes. Though these optical modes were initially attributed to the excitation of LO phonon modes [56], later research showed that these modes correspond to phonon-polariton in polar-dielectrics that fall within the light cone and a surface mode beyond the light cones that are characterized with a real wave vector and complex frequency [44].

The reflectivity (R) spectrum of the 200 nm AlN deposited on 100 nm TiN, indeed, shows the coupling of incident light with the Berreman modes with a sharp dip in the reflection at 891 cm^{-1} that is very close to AlN's LO phonon frequency (see Fig. 5(b)). The FWHM of the absorption peak corresponding to the Berreman peak is 32 cm^{-1}, resulting in a *Q*-factor of 28. The reflectivity (R) spectrum also shows a dip at 673 cm^{-1} that is close to the TO phonon frequency of AlN and represents the direct light coupling to the TO mode of AlN. The Fresnel equation is modified to model the reflectivity spectrum, and a Berreman term [56] is included. The total reflection coefficient is obtained by using equation (2)

$$R = R_{Fresenal} \times R_{Berreman} = \left|\frac{r_{12} + r_{23}e^{2ik_{z2}d}}{1 + r_{12}\, r_{23}e^{2ik_{z2}d}}\right|^2 \left[1 - 4\delta\left(\frac{Im\,(\varepsilon_{PD})}{Re\,(\varepsilon_{PD})^2 + Im\,(\varepsilon_{PD})^2}\right)\right] \quad (2)$$

where the first term ($R_{Fresenal}$) represents reflectivity for the three-layer system by utilizing the Maxwell's equation, r_{ij} is the complex reflection coefficient between layers i and j (with layers 1, 2, and 3 referring to air, AlN, and TiN, respectively), and k_{zi} is the wavevector component of light in the ith layer. The second term ($R_{Berreman}$) is Berreman's term to explain light absorption near to the LO mode of AlN, and ε_{PD} is the permittivity of AlN

$$\varepsilon_{PD} = \varepsilon_\infty\left(1 + \frac{\omega_{LO}{}^2 - \omega_{TO}{}^2}{\omega_{TO}{}^2 - \omega^2 - i\omega\Gamma}\right) \quad (3)$$

Here the ω_{LO} (ω_{TO}) is the LO (TO) phonon frequencies of AlN respectively, Γ is the damping of the phonons, and $\delta/2\pi$ is the thickness of the dielectric film, measured in vacuum wavelengths of the incident radiation. Fig. 5(b) show that the modeled reflectivity spectrum matches well with the experimental results.

Further, $Al_{0.72}Sc_{0.28}N$ layers with thicknesses of 100 nm and 1000 nm (1 μm) are deposited on 100 nm TiN, respectively and their reflection spectra are measured. For both $Al_{0.72}Sc_{0.28}N$ films, light coupling to the Berreman modes is observed at ~895 cm^{-1} (see Fig. 5(c)), which is close to AlN's LO phonon frequency. As mentioned previously, the inclusion of scandium inside AlN does not impact the high-frequency LO modes due to the higher atomic mass of scandium atoms. The absorption measurements, therefore, confirm it. Reflection spectra of 1 μm $Al_{0.72}Sc_{0.28}N$ film also show the light coupling to the TO optical phonon mode at 565 cm^{-1} at a slightly smaller frequency than AlN. Optical phonon modes in $Al_xS_{1-x}cN$ have been studied in detail and similar consequence has been seen in the previous reports [70]. The broadening and shift of the mode frequencies can unambiguously be attributed to an elongation of Al (Sc)-N bonds because of Sc doping. Contrary to that, 100 nm $Al_{0.72}Sc_{0.28}N$ film show almost no reflection dip at the TO phonon frequency. This behavior was also observed previously for thin AlN layers deposited on metallic Mo layers [71] due to the small optical path length for the light to couple with the sample's TO phonon. It is important to note that though the absorption peaks in AlN and $Al_{0.72}Sc_{0.28}N$ are located near to one another, the FWHM of the $Al_{0.72}Sc_{0.28}N$ peaks is much broader than that of AlN's absorption peak. Compared to the AlN absorption peak FWHM of 14 cm^{-1} (for TO) and 32 cm^{-1} (for LO), $Al_{0.72}Sc_{0.28}N$ exhibits a much larger FWHM of 103 cm^{-1} (for TO) and 102 cm^{-1} (for LO). Such higher FWHM results from higher damping constant of $Al_{0.72}Sc_{0.28}N$ with respect to AlN, leading to $Al_{0.72}Sc_{0.28}N$'s smaller resonance *Q*-factor. Since the inclusion of scandium inside AlN is necessary to achieve rocksalt-$Al_{0.72}Sc_{0.28}N$ with lattice-matched interfaces, there seems to be a tread-off between the structural requirements for stable epitaxial film and high-quality optical resonance.

The spectral response of the Berreman modes can be further calculated [71] in the limit of optically thin $Al_{0.72}Sc_{0.28}N$ layers.

$$\varepsilon_{PD}k_{z1} + idk_{z2}^2 = 0 \quad (4)$$

The dispersion spectrum (see Fig. 5(d)) shows that the thin 100 nm $Al_{0.72}Sc_{0.28}N$ layer exhibits close to angle independent Berreman mode frequencies. Whereas 1 μm $Al_{0.72}Sc_{0.28}N$ exhibits a much dispersive Berreman mode spectral response. Though the experiments are performed for a fixed angle of incident, the Berreman mode frequencies in the experiment and in the dispersion spectrum match with each other.

Therefore, this study demonstrates that the metal-polar dielectric-metal multilayer structures can provide dual optical resonances at two different spectral regimes. The cavity resonance governs the optical absorption in the visible-to-NIR spectral range, while excitation of the TO phonon and the Berreman modes leads to light absorption in the mid-to-long wavelength infrared regime. In addition, we achieve both of these resonances utilizing refractory epitaxial and CMOS-compatible TiN as the plasmonic and $Al_{0.72}Sc_{0.28}N$ as the polar-dielectric layer that overcomes many of the material challenges that noble metal-based optical structures encounter. Though the present work exhibit optical resonances in the 580 nm–1200 nm for the visible-to-NIR and 10.5 μm–13 μm in the mid-to-long wavelength IR spectral ranges, the structures could be further optimized to achieve the resonances at specific wavelengths necessary for radiative cooling and thermophotovoltaic applications.

In conclusion, we show simultaneous light-matter interaction and optical resonance in the visible and mid-IR spectral range with a lithography-free planar wide-angle TiN/$Al_{0.72}Sc_{0.28}N$/TiN metal-(polar)-dielectric-metal (MDM) Fabry-Pérot cavity. Tunable super absorption with absorptivity exceeding 99% is achieved in the 580 nm–1200 nm spectral range by varying the dielectric layer thickness inside the MDM cavity. Splitting of the cavity modes through interactions between multiple cavities is also demonstrated as a method to tailor the optical absorption in the visible-to-near-IR spectral region. The MDM metamaterials are shown to exhibit mid-to-long IR light absorption due to the direct light coupling not only to the transverse optical (TO) phonon modes but also to the leaky polaritonic Berreman modes. Detailed analysis of the Reststrahlen bands in AlN and $Al_{0.72}Sc_{0.28}N$ along with the spectral response of the Berreman mode is further demonstrated. Demonstration of optical absorption and simultaneous light-matter coupling in the visible and in the mid-to-long wavelength IR spectral range with a single metamaterial mark important progress in the quest to design functional optical materials that can be used for energy conversion, sensing, healthcare, security and other applications.

Credit author statement

Krishna Chand Maurya: Conceptualization, Methodology, Data curation, Writing- Original draft preparation. Ashalatha Indiradevi Kamalasanan Pillai: Data curation, Visualization, Investigation, Magnus Garbrecht: Data curation, Visualization, Investigation, and Bivas Saha: Conceptualization, Methodology, Writing- Reviewing and Editing.

Data availability statement

The data that supports the findings of this study are available from the corresponding author upon reasonable request.

Declaration of competing interest

The authors declare that they have no known competing financial interests or personal relationships that could have appeared to influence the work reported in this paper.

Acknowledgments

KCM, and BS acknowledge International Center for Materials Science (ICMS) and Sheikh Saqr Laboratory (SSL) in JNCASR for support. B.S. acknowledges the Sheikh Saqr Laboratory (SSL) in JNCASR of the Government of India, Start-Up Research Grant No. SRG/2019/000613 for financial support. KCM thank Council of Scientific & Industrial Research (CSIR) for fellowship. M.G. and AIKP acknowledges the facilities of Sydney Microscopy and Microanalysis at The University of Sydney.

Appendix A. Supplementary data

Supplementary data to this article can be found online at https://doi.org/10.1016/j.mtphys.2022.100797.

References

[1] H.A. Atwater, A. Polman, Nat. Mater. 9 (2010) 205–213.
[2] V.C. Nikolis, A. Mischok, B. Siegmund, J. Kublitski, X. Jia, J. Benduhn, U. Hörmann, D. Neher, M.C. Gather, D. Spoltore, K. Vandewal, Nat. Commun. 10 (2019) 1–8.
[3] S. An, Y. Liao, M. Kim, ACS Appl. Mater. Interfaces 13 (2021) 61396–61403.
[4] B. Hou, L. Shen, H. Shi, R. Kapadia, S.B. Cronin, Phys. Chem. Chem. Phys. 19 (2017) 2877–2881.
[5] F. Li, R. Tao, B. Cao, L. Yang, Z. Wang, Adv. Funct. Mater. 31 (2021): 2104367.
[6] M.K. Kwon, J.Y. Kim, B.H. Kim, I.K. Park, C.Y. Cho, C.C. Byeon, S.J. Park, Adv. Mater. 20 (2008) 1253–1257.
[7] R.K. Vinnakota, Z. Dong, A.F. Briggs, S.R. Bank, D. Wasserman, D.A. Genov, Nanophotonics 9 (2020) 1105–1113.
[8] C. Haffner, D. Chelladurai, Y. Fedoryshyn, A. Josten, B. Baeuerle, W. Heni, T. Watanabe, T. Cui, B. Cheng, S. Saha, D.L. Elder, L.R. Dalton, A. Boltasseva, V. M. Shalaev, N. Kinsey, J. Leuthold, Nature 556 (2018) 483–486.
[9] M.M. Hossain, B. Jia, M. Gu, Adv. Opt. Mater. 3 (2015) 1047–1051.
[10] Y. Zhai, Y. Ma, S.N. David, D. Zhao, R. Lou, G. Tan, R. Yang, X. Yin, Science 355 (80-) (2017) 1062–1066.

[11] C.C. Chang, W.J.M. Kort-Kamp, J. Nogan, T.S. Luk, A.K. Azad, A.J. Taylor, D.A. R. Dalvit, M. Sykora, H.T. Chen, Nano Lett. 18 (2018) 7665–7673.
[12] M. Chirumamilla, A. Chirumamilla, Y. Yang, A.S. Roberts, P.K. Kristensen, K. Chaudhuri, A. Boltasseva, D.S. Sutherland, S.I. Bozhevolnyi, K. Pedersen, Adv. Opt. Mater. 5 (2017).
[13] S. Molesky, C.J. Dewalt, Z. Jacob, Opt Express 21 (2013) 549–554.
[14] T. Nikolajsen, K. Leosson, S.I. Bozhevolnyi, Appl. Phys. Lett. 85 (2004) 5833–5835.
[15] R.A. Lewis, J. Phys. D Appl. Phys. 52 (2019): 433001.
[16] C. Corsi, Adv. Opt. Technol. (2012), 2012.
[17] D. Sanvitto, S. Kéna-Cohen, Nat. Mater. 15 (2016) 1061–1073.
[18] J.D. Caldwell, I. Vurgaftman, J.G. Tischler, O.J. Glembocki, J.C. Owrutsky, T. L. Reinecke, Nat. Nanotechnol. 11 (2016) 9–15.
[19] K.C. Maurya, B. Biswas, D. Rao, B. Saha, Appl. Phys. Lett. 118 (2021): 041902.
[20] G.V. Naik, V.M. Shalaev, A. Boltasseva, Adv. Mater. 25 (2013) 3264–3294.
[21] S.A. Maier, Plasmon. Fundam. Appl., Springer US, New York, NY, 2007, pp. 39–52.
[22] K. Aydin, V.E. Ferry, R.M. Briggs, H.A. Atwater, Nat. Commun. 2 (2011) 1–7.
[23] X. Chen, H. Gong, S. Dai, D. Zhao, Y. Yang, Q. Li, M. Qiu, Opt. Lett. 38 (2013) 2247.
[24] L. Zhou, Y. Tan, D. Ji, B. Zhu, P. Zhang, J. Xu, Q. Gan, Z. Yu, J. Zhu, Sci. Adv. 2 (2016) 1–8.
[25] C. Fei Guo, T. Sun, F. Cao, Q. Liu, Z. Ren, Light Sci. Appl. 3 (2014) e161–e161.
[26] K.-T. Lin, H. Lin, B. Jia, Nanophotonics 9 (2020) 3135–3163.
[27] T.D. Dao, K. Chen, S. Ishii, A. Ohi, T. Nabatame, M. Kitajima, T. Nagao, ACS Photonics 2 (2015) 964–970.
[28] A. Tittl, A.K.U. Michel, M. Schäferling, X. Yin, B. Gholipour, L. Cui, M. Wuttig, T. Taubner, F. Neubrech, H. Giessen, Adv. Mater. 27 (2015) 4597–4603.
[29] N.I. Landy, S. Sajuyigbe, J.J. Mock, D.R. Smith, W.J. Padilla, Phys. Rev. Lett. 100 (2008): 207402.
[30] A. Kavokin, J.J. Baumberg, G. Malpuech, F.P. Laussy, Microcavities, second ed., oxford university press, 2008.
[31] Z. Wang, J.K. Clark, Y.L. Ho, B. Vilquin, H. Daiguji, J.J. Delaunay, ACS Photonics 5 (2018) 2446–2452.
[32] D.G. Baranov, A. Krasnok, T. Shegai, A. Alù, Y. Chong, Nat. Rev. Mater. 2 (2017): 17064.
[33] Y. Wang, L. Zhou, Y. Zhang, J. Yu, B. Huang, Y. Wang, Y. Lai, S. Zhu, J. Zhu, Adv. Opt. Mater. 6 (2018) 1–7.
[34] M. Hentschel, J. Karst, H. Giessen, Adv. Opt. Mater. 8 (2020): 2000879.
[35] J.D. Caldwell, L. Lindsay, V. Giannini, I. Vurgaftman, T.L. Reinecke, S.A. Maier, O. J. Glembocki, Nanophotonics 4 (2015) 44–68.
[36] S. Foteinopoulou, G.C.R. Devarapu, G.S. Subramania, S. Krishna, D. Wasserman, Nanophotonics 8 (2019) 2129–2175.
[37] G. Hu, J. Shen, C.W. Qiu, A. Alù, S. Dai, Adv. Opt. Mater. 8 (2020) 1–19.
[38] S.S. Ng, Z. Hassan, H. Abu Hassan, Appl. Phys. Lett. 90 (2007) 2005–2008.
[39] R. Hillenbrand, T. Taubner, F. Keilmann, Nature 418 (2002) 159–162.
[40] K. Torii, T. Koga, T. Sota, T. Azuhata, S.F. Chichibu, S. Nakamura, J. Phys. Condens. Matter 12 (2000) 7041–7044.
[41] K.C. Maurya, D. Rao, S. Acharya, P. Rao, A.I.K. Pillai, S.K. Selvaraja, M. Garbrecht, B. Saha, Nano Lett. 22 (13) (2022) 5182–5190, https://doi.org/10.1021/acs.nanolett.2c00912.
[42] K.C. Maurya, B. Biswas, M. Garbrecht, B. Saha, Phys. Status Solidi Rapid Res. Lett. 13 (2019): 1900196.
[43] M.A. Stroscio, M. Dutta, Phonons in Nanostructures, Cambridge University Press, 2001, pp. 16–25.
[44] S. Vassant, J.-P. Hugonin, F. Marquier, J.-J. Greffet, Opt Express 20 (2012): 23971.
[45] I. Khan, Z. Fang, M. Palei, J. Lu, L. Nordin, E.L. Simmons, O. Dominguez, S. M. Islam, H.G. Xing, D. Jena, V.A. Podolskiy, D. Wasserman, A.J. Hoffman, Opt Express 28 (2020): 28590.
[46] L.D. Yau, C.T. Sah, Appl. Phys. Lett. 21 (1972) 157–158.
[47] M.N. Gadalla, K. Chaudhary, C.M. Zgrabik, F. Capasso, E.L. Hu, Opt Express 28 (2020): 14536.
[48] K.C. Maurya, V.M. Shalaev, A. Boltasseva, B. Saha, Opt. Mater. Express 10 (2020) 2679.
[49] R.V. Babinova, V.V. Smirnov, A.S. Useenov, K.S. Kravchuk, E.V. Gladkikh, V. I. Shapovalov, I.L. Mylnikov, J. Phys. Conf. Ser. 872 (2017): 012035.
[50] X. Pang, L. Zhang, H. Yang, K. Gao, A.A. Volinsky, J. Mater. Eng. Perform. 24 (2015) 1185–1191.
[51] B. Saha, G.V. Naik, S. Saber, C. Akatay, E.A. Stach, V.M. Shalaev, A. Boltasseva, T. D. Sands, Phys. Rev. B 90 (2014): 125420.
[52] M. Garbrecht, L. Hultman, M.H. Fawey, T.D. Sands, B. Saha, J. Mater. Sci. 53 (2018) 4001–4009.
[53] J.L. Schroeder, B. Saha, M. Garbrecht, N. Schell, T.D. Sands, J. Birch, J. Mater. Sci. 50 (2015) 3200–3206.
[54] M. Garbrecht, L. Hultman, M.H. Fawey, T.D. Sands, B. Saha, Phys. Rev. Mater. 1 (2017): 033402.
[55] B. Saha, S. Saber, E.A. Stach, E.P. Kvam, T.D. Sands, Appl. Phys. Lett. 109 (2016): 172102.
[56] D.W. Berreman, Phys. Rev. 130 (1963) 2193–2198.
[57] V. Caligiuri, M. Palei, G. Biffi, S. Artyukhin, R. Krahne, Nano Lett. 19 (2019) 3151–3160.
[58] V. Caligiuri, M. Palei, G. Biffi, R. Krahne, Nanophotonics 8 (2019) 1505–1512.
[59] Z. Li, S. Butun, K. Aydin, ACS Photonics 2 (2015) 183–188.
[60] J. Kim, H. Oh, M. Seo, M. Lee, ACS Photonics 6 (2019) 2342–2349.
[61] A. Ghobadi, H. Hajian, B. Butun, E. Ozbay, ACS Photonics 5 (2018) 4203–4221.
[62] A.S. Roberts, M. Chirumamilla, D. Wang, L. An, K. Pedersen, N.A. Mortensen, S. I. Bozhevolnyi, Opt. Mater. Express 8 (2018) 3717.
[63] M. Aalizadeh, A. Khavasi, B. Butun, E. Ozbay, Sci. Rep. 8 (2018) 1–13.
[64] J. Kuttruff, D. Garoli, J. Allerbeck, R. Krahne, A. De Luca, D. Brida, V. Caligiuri, N. Maccaferri, Commun. Phys. 3 (2020) 1–7.
[65] Q. Li, T. Wang, Y. Su, M. Yan, M. Qiu, Opt Express 18 (2010) 8367.
[66] M. Bayer, T. Gutbrod, J.P. Reithmaier, A. Forchel, T.L. Reinecke, P.A. Knipp, A. A. Dremin, V.D. Kulakovskii, Phys. Rev. Lett. 81 (1998) 2582–2585.
[67] K. Liao, X. Hu, T. Gan, Q. Liu, Z. Wu, C. Fan, X. Feng, C. Lu, Y. Liu, Q. Gong, Adv. Opt Photon 12 (2020) 60.
[68] A.F. Turner, L. Chang, T.P. Martin, Appl. Opt. 4 (1965) 927.
[69] V.Y. Davydov, Y.E. Kitaev, I. Goncharuk, A. Smirnov, J. Graul, O. Semchinova, D. Uffmann, Phys. Rev. B Condens. Matter 58 (1998) 12899–12907.
[70] R. Deng, K. Jiang, D. Gall, J. Appl. Phys. 115 (2014): 013506.
[71] L. Nordin, O. Dominguez, C.M. Roberts, W. Streyer, K. Feng, Z. Fang, V. A. Podolskiy, A.J. Hoffman, D. Wasserman, Appl. Phys. Lett. 111 (2017) 91105.